Final Draft
of the original manuscript:

Srinivasan, P.B.; Arora, K.S.; Dietzel, W.; Pandey, S.; Schaper, M.K.:
Characterisation of microstructure, mechanical properties and corrosion behaviour of an AA2219 friction stir weldment
In: Journal of Alloys and Compounds (2009) Elsevier

DOI: 10.1016/j.jallcom.2009.11.198

Characterisation of microstructure, mechanical properties and corrosion behaviour of an AA2219 friction stir weldment

P. Bala Srinivasan[1,*], K.S. Arora[2], W. Dietzel[1], S. Pandey[2], M.K. Schaper[3]

[1] Institute of Materials Research
GKSS-Forschungszentrum Geesthacht GmbH
D-21502 Geesthacht, Germany

[2] Department of Mechanical Engineering
Indian Institute of Technology
New Delhi, 110 016, India

[3] Institute of Materials Science
Technical University of Dresden
D-10602, Dresden, Germany

*Corresponding Author (bala.srinivasan@gkss.de);
Phone: 00-49-4152-871997; Fax: 00-49-4152-871960

Keywords: Aluminium alloy; Friction stir weld; Hardness; Electrochemical behaviour; Stress corrosion cracking; Slow strain rate tensile test.

Abstract

A friction-stir weldment of AA2219-T87 aluminium alloy was characterized for its microstructure, mechanical properties, corrosion resistance and stress corrosion cracking behaviour. The dissolution and coarsening of the strengthening precipitates in the weld nugget and TMAZ/HAZ regions, respectively, had resulted in the softening of these regions; nevertheless, the weld joint was found to have an efficiency of around 72%. The general corrosion behaviour of the weld nugget was superior to that of the parent. The TMAZ/HAZ regions, and the weld nugget were found to have been galvanically protected in the immersion tests. Both the parent alloy and the friction stir weldment specimens exhibited a good resistance to stress corrosion cracking in 3.5% NaCl solution as was demonstrated by slow strain rate tensile tests performed at nominal strain rates of 10^{-6} s^{-1} and 10^{-7} s^{-1}.

1. Introduction

Age-hardenable aluminium-copper alloys are widely used for aircraft and aerospace applications owing to their excellent mechanical properties and good strength-to-weight ratio. Friction stir welding (FSW) has been a preferred process for the joining of the so-called difficult-to-weld heat-treatable aluminium alloys right since its inception in the year 1991 **[1-2]**. This solid state welding process overcomes the issues of liquation cracking, porosity and distortion in the weldments which are often associated with the other welding processes viz. gas tungsten arc welding (GTAW) and gas metal arc welding (GMAW) **[3-6]**. High-strength aluminium alloy weldments obtained by FSW were reported to possess good mechanical properties and were found to exhibit better joint efficiency than GTA/GMA weldments **[7-9]**. The joining of AA2219 alloy in different temper conditions was carried out by Chen et al. using FSW, and their microstructure–mechanical property correlation was well documented **[10-11]**. The evolution of fine grained structure in the friction stir welds partly compensates for the dissolution and/or coarsening of the strengthening precipitates in the weld nugget, and thus provides better mechanical properties than those realised in the GTA welds. The corrosion and stress corrosion cracking (SCC) behaviour of various high strength aluminium alloys and also that of dissimilar weldments comprising two different aluminium alloys have been investigated by many researchers **[12-17]**. Paglia and Buchheit in their recent viewpoint paper reviewed the corrosion of aluminium alloy friction welds and reported the sensitization of the microstructure during welding as the responsible factor for the decrease in the corrosion resistance of weld nugget and heat-affected zone in friction stir weldments **[18]**. Further, the environmental cracking behaviour and the regions of susceptibility in the friction stir weldments of different aluminium alloys were reported to be influenced by the microstructure and chemistry. As there is not much published information on the corrosion and SCC behaviour AA2219 aluminium alloy friction stir welds, except a few **[19-20]**, the present work is aimed at the understanding of the

corrosion and SCC behaviour of an AA2219-T87 alloy friction-stir weldment in the as-welded condition in chloride environments.

2. Experimental

A 5 mm thick wrought AA2219 aluminium alloy plate with a nominal chemical composition (wt.%) of Cu 5.95%, Mn 0.27%, Zr 0.1%, V 0.09%, Ti 0.06%, Fe 0.12%, Si 0.05% and balance Al was used in this investigation. The alloy was received in the T87 temper, after having been subjected to the following heat treatment: solutionized at 535°C for 45 minutes followed by cold rolling and a subsequent aging treatment at 165°C for 24 hours to obtain a stabilised microstructure.

FSW was carried out at Hi-Tech Vocational Training Centre (HTVTC), Okhla, New Delhi. The welds were made in a CNC friction-stir welding machine by joining two plates of size 5 mm × 50 mm × 250 mm to make a welded part of 100 mm wide and 250 mm long. The FSW tool was made of H13 steel in the quenched and tempered condition, with a hardness value of 45 HRC. All the welds were produced with the following optimised welding parameters: axial load – 10.6 kN, tool rotation – 400 RPM, pin diameter – 7 mm, shoulder diameter – 20 mm, welding speed – 180 mm/min.

Specimens for the metallographic observations were prepared by polishing successively using 220, 400, 1000, 1200 and 2500 grit emery sheets followed by disc polishing in diamond slurry (1 µm). Final polishing was carried out in 0.5 µm colloidal silica solution, and then the specimens were etched using Keller's reagent for appropriate durations for the macro and microstructural examinations. Transmission electron microscopy (TEM) analysis of the parent and weld nugget regions were performed on thin-foil specimens prepared in a twin-jet polisher at -20°C using 30% nitric acid in methanol. The specimens were examined in a Zeiss TEM (EM912 Omega, LaB6 cathode) operated at 120 kV. Micro hardness measurements were made across the weld joint as traverse

survey, at three locations viz., 0.5 mm below the face of weld (top surface), 2.5 mm (mid-thickness) and 4.5 mm below the face of weld (i.e. 0.5 mm from weld root) with 1 N load and a dwell time of 20s.

The electrochemical behaviour of the parent, TMAZ/HAZ and weld nugget regions was assessed using a Gill AC potentiostat. The free corrosion potential of the different regions was measured for 10 minutes on the specimens polished to 2500 grit emery finish. Subsequently, the specimens were subjected to the potentiodynamic polarisation test (in triplicate) using a three electrode cell in which the test specimen, an Ag/AgCl electrode (containing saturated KCl solution with a potential of 0.199 V w.r.t. the standard hydrogen electrode), and a platinum mesh were employed as working, reference and auxiliary electrodes, respectively, at a sweep rate of 0.5 mV s^{-1} in non-deaerated 3.5% NaCl solution. The friction stir weldment specimen of size 5 mm x 40 mm x 50 mm, comprising the weld nugget, TMAZ/HAZ and parent was also subjected to an immersion test in a solution containing 57 g of NaCl and 10 ml of hydrogen peroxide in 1 L of distilled water for 6 hours. Even though the test procedure recommended by ASTM G110-92 is for the assessment of intergranular corrosion of aluminium alloys, it was used in this investigation to understand the galvanic corrosion effects.

AA2219-T87 parent alloy and the friction stir weldment flat tensile specimens with gauge section of 5 mm x 22 mm were subjected to slow strain rate tensile (SSRT) tests in 3.5% NaCl solution at two nominal strain rates, viz., 10^{-6} s^{-1} and 10^{-7} s^{-1}. The weldment specimen was in the transverse section and the gauge section contained the weld nugget, TMAZ and HAZ regions. Reference tests were performed in air at 10^{-6} s^{-1}. The specimen elongation in all the SSRT tests was measured using two linear variable displacement transducers (LVDT) attached to the specimen grips. As the elongation was not measured with clip-on-gauges exactly from the gauge section but only with

these LVDTs, it is referred to as “apparent strain” in the discussion. The SSRT tested specimens were examined in an optical microscope and in a scanning electron microscope for identifying the fracture location in the weldments and to assess the fracture surface appearance, respectively.

3. Results and discussion

3.1 Microstructure and hardness

Optical macrograph of the cross-section of the friction stir weldment is shown in **Figure 1**. The micrograph of the parent alloy shown in **Figure 2** reveals elongated grains characteristic of the rolled material, with some dark intermetallic particles. The densely distributed plate-like semi-coherent and coherent strengthening precipitates observed in the parent alloy are shown in the transmission electron micrograph shown in **Figure 3a**, and the higher magnification of micrograph shown in **Figure 3b** clearly reveals the morphology of these precipitates. The weld nugget of the weldment obtained under the optimised welding conditions was found to comprise two distinctly different regions. The features of the fine re-crystallized structure observed in the upper region (region A in Figure 1) and the bottom region (region B in Figure 1) of the weld nugget are shown in **Figure 4a** and **Figure 4b**, respectively. The size of grains in the weld nugget were in the range 2 – 8 μm, with the grains in the in the bottom half of the weld being finer compared to the upper half of the weld, as can be observed from these figures. Chen et al. **[11, 21]** reported the formation of such structure with onion rings, but from the macrographs in those publications the structure appears to be uniform across the thickness of weld nugget. A representative transmission electron micrograph of the weld nugget obtained in this work shown in **Figure 5a** gives an account of the grain size and precipitates in this region. The dislocation density is evidently higher in the weld nugget due to the extensive plastic deformation and flow of material during welding. The plate-like precipitates observed in the parent alloy are completely absent

in the nugget region as can be observed in the higher magnification TEM micrograph in **Figure 5b**. Similar observations were made and reported by Chen et al. **[21]** in their work on FSW of AA2219 aluminium alloy.

Figure 6 shows the micro-hardness traverse across the weld joint obtained at three different locations viz., 0.5 mm, 2.5 mm and 4.5 mm from the face of the weld (top surface) as hardness line-scans. The hardness of the weld nugget region was in the range of 85 – 110 $HV_{0.5}$ and the variation in hardness across the thickness direction in the weld nugget was marginal. The hardness of the TMAZ/HAZ region adjoining the weld nugget was lower than that of the nugget region with some overlap, registering values in the range 80 – 90 $HV_{0.5}$. The hardness of the parent alloy was found to be 155 $\pm$ 5 $HV_{0.5}$ and the hardness gradient between the parent and the TMA/HAZ region was found to be steep. The uniform hardness distribution across the section thickness of the weld nugget suggests that the perceptible variations in the grain size in the weld nugget did not have any great influence on the hardness of the weld nugget.

3.2 Corrosion behaviour

The measurement of the open circuit potential (OCP) of the parent alloy, TMAZ/HAZ and the weld nugget regions in 3.5% NaCl solution was performed for 10 minutes before the polarisation studies **(Figure 7a)**. The parent alloy exhibited a potential of around -635 mV vs. Ag/AgCl and that of the TMAZ/HAZ and weld nugget regions were in the range -595 $\pm$ 5 mV and -565 $\pm$ 5 mV vs. Ag/AgCl, respectively. Both the TMAZ/HAZ and the weld nugget specimens showed a slight drift of potential towards the active side with increase in immersion time, as is evident from Figure 7a. The potentiodynamic polarisation behaviour of the three regions of the weldment is shown in **Figure 7b**. The E_{corr} values of the parent, TMAZ/HAZ and the weld nugget regions were -605 mV, -575 mV and -525 mV vs. Ag/AgCl, respectively. The corrosion current

density value (i_{corr}) registered for the parent alloy was 2.0 μA cm^{-2} as against 1.7 μA cm^{-2} and 1.2 μA cm^{-2} for the TMAZ/HAZ and weld nugget regions, respectively. A better corrosion resistance of TMAZ/HAZ and the weld nugget regions in 2xxx series aluminium alloys have been reported earlier **[19-20]**. The dissolution of precipitates in the weld nugget and the coarsening of precipitates in the TMAZ/HAZ regions seem to be the responsible factors for the improved corrosion resistance as well as the nobler corrosion potentials of these two regions.

The weldment specimen polished to 2500 grit emery finish was subjected to an immersion test as per ASTM G110-93 in a solution containing NaCl + H_2O_2. Even though this is a recommended test for the assessment of intergranular corrosion of aluminium alloys, in this investigation we performed this test to assess the galvanic corrosion behaviour of the weldment. The optical macrograph of the FSW specimen in **Figure 8** shows the extent of corrosion damage on the different regions of the weldment. The weld nugget seems to have turned into a cathode and was completely protected from corrosion damage. The cathodic reaction on the weld nugget region had resulted in the discoloration of the surface. The TMAZ/HAZ region was also more or less free from corrosion damage. On the other hand, the parent alloy was found to have been severely attacked. Examination of the corroded region in an optical microscope after removal of corrosion products revealed that the corrosion attack on the parent alloy was extensively intergranular. The corrosion behaviour is attributed to the galvanic effect that could be understood from the polarisation plots of the weld nugget, TMAZ/HAZ and the parent alloy regions presented in Figure 7(b). It is evident that the TMAZ/HAZ and the weld nugget regions were nobler than the parent alloy. Hence, when this weldment with the composite regions (parent-TMAZ/HAZ-weld nugget) was exposed to the corrosive environment, the parent alloy with a relatively more active free corrosion potential became anode and underwent an active dissolution. This was in a

way governed by the evolution of the mixed potential (galvanic potential) dictated by the other two cathodic regions, viz., TMAZ/HAZ and weld nugget. Thus, when the weldment was exposed to the corrosive environment, the corrosion damage occurred only at the anodic region viz., parent alloy and the rest of the regions were cathodically protected. Free corrosion potential measurements of the parent alloy, TMAZ/HAZ and weld nugget regions made in NaCl + H_2O_2 solution also has shown a very similar trend as was observed in neutral 3.5% NaCl solution.

3.3 Stress corrosion cracking (SCC) behaviour

Before assessing the SCC behaviour of the parent alloy and the weldment specimens, they were subject to slow strain rate tensile (SSRT) tests in air at 10^{-6} s^{-1}. The stress vs. apparent strain plots obtained for the parent and FSW specimens (in air) are shown in **Figure 9**. The ultimate tensile strength (UTS) values of the parent and FSW specimens were 445 MPa and 320 MPa, respectively and the apparent strain values were around 22% for both the cases. The efficiency of the friction stir weld joint obtained in this work was 72%. Chen et al. **[11]** reported a joint efficiency of 82% for the FSW joints of AA2219 in T6 temper. Paglia and Buchheit **[20]** have observed a joint efficiency of around 74% in the FSW joints of AA2219 in T87 temper, but the UTS values were only around 350 MPa and 260 MPa for the parent and FSW specimens, respectively. However, since the exact welding parameters and heat treatment history of that work was not disclosed, it is difficult to comment on the lower strength levels and elongation values reported by them. The work on the electron beam (EB) and gas tungsten arc (GTA) welding of AA2219-T87 alloy by Koteswara Rao et al. **[22]** reported UTS values of 327 MPa and 229 MPa for the EB and GTA welds, respectively, with an elongation value of only around 5%. Thus, the combination of mechanical properties (strength and elongation) of the weldment produced in current work is better than those for AA2219 alloy weldments reported by other researchers.

The optical macrograph of the SSRT tested specimen in air shown in **Figure 10a** reveals the deformation in the nugget/TMAZ region in the weldment. Whilst the fracture seems to have been confined to the weld nugget region as it appears in Figure 10a, the higher magnification micrograph shown in **Figure 10b** demonstrates that the crack propagated along the weld nugget/TMAZ interface in the weldment. The micro hardness survey performed on this weldment suggested that the weld nugget/TMAZ interface is the softest zone in the weldment, and thus the fracture in this region in the tensile test is not a surprise. The scanning electron fractograph from the face region of the nugget (region marked (i) in Figure 10a) showed a fine dimpled structure **(Figure 11a)**, and that from the root region (TMAZ region marked (ii) in Figure 10a) exhibited a relatively coarse dimpled fracture surface **(Figure 11b)**. The fracture surface of the parent alloy also contained similar features as that seen in Figure 11b.

The stress vs. apparent strain plots of the AA2219 parent alloy and the FSW specimens tested in 3.5% NaCl solution at two strain rates are presented in **Figure 12**. The UTS values of the parent alloy tested at 10^{-6} s^{-1} and 10^{-7} s^{-1} were 440 MPa and 425 MPa, respectively, and the apparent strain values were around 22% in both the cases. The time to failure of the parent alloy in the SSRT tests in air and in 3.5% NaCl solution at 10^{-6} s^{-1} was approximately 55 hours and that in the test at 10^{-7} s^{-1} was around 525 hours. The fracture surface of the specimens tested in air and in solution at 10^{-6} s^{-1} showed dimpled structure, suggesting a ductile failure. The scanning electron fractograph of the parent specimens tested at 10^{-7} s^{-1} shown in **Figure 13** reveals a fracture surface with dimples and some corrosion damage, as well. Even though the SCC susceptibility index (I_{SCC}-UTS), which is the ratio of UTS in corrosive environment and UTS in air) for the specimen tested at 10^{-7} s^{-1} was 0.96, there was no distinct evidence of SCC from the fractographic analysis.

In the case of the FSW specimens SSRT tested at 10^{-6} s^{-1} the time to failure was around 55 hours in the tests in air and in 3.5% NaCl solution and in both the cases the apparent strain before fracture was around 22%. The UTS values of the FSW specimens tested in solution were around 300 MPa in the tests performed at 10^{-6} s^{-1} and 10^{-7} s^{-1}, yielding a I_{SCC}-UTS of approximately 0.95, a value very similar to that observed for the parent alloy. The apparent strain to failure was also nearly the same for both the cases with values of around 22% and 20.5% for the specimens SSRT tested at 10^{-6} s^{-1} and 10^{-7} s^{-1}, respectively. The optical macrograph of the representative SSRT FSW specimen tested at 10^{-7} s^{-1} shown in **Figure 14** reveals that the fracture was in the weld nugget/TMAZ regions and that in this case the fracture was not at 45°. The deformation/necking of the nugget/TMAZ region could also clearly be seen, even though its extent was not exactly the same as that of the specimen tested in air as is seen in Figure 10a. The electrochemical corrosion studies and the immersion tests in NaCl + H_2O_2 solution suggested that the weld nugget region had the best corrosion resistance. Nevertheless, in the SSRT tests in the corrosive solution the fracture/failure was noticed in the weld nugget/TMAZ region. The higher magnification micrographs of the regions marked as (i) and (ii) in Figure 14, presented in **Figures 15a** and **15b**, reveal that the surfaces of the weld nugget and the TMAZ/HAZ contained numerous cracks. Due to the prolonged exposure to the electrolyte during the SSRT test the surface of the entire gauge section of the specimen was covered with a film and this film was damaged due to the slow straining of the specimen when stressed beyond yield strength of the alloy/weldment and was plausibly assisted by chloride ions. Thus, the defective sites created on the surface had nucleated localised pits, which subsequently have grown as cracks. Similar cracks were observed in the parent alloy, too, in the SSRT tests in corrosive environment. Nevertheless, both the parent alloy and the FSW specimens were found to be resistant to the crack propagation and these cracks did not cause catastrophic stress corrosion cracking at a strain rate of 10^{-7} s^{-1}. The scanning

electron fractograph of the SSRT tested FSW specimen obtained from the root region of the weld (failure region TMAZ) presented in **Figure 16** reveals a dimpled structure in the grains and also some regions with corrosion damage, the features which were very similar to those noticed in the parent alloy SSRT tested in 3.5% NaCl solution at 10^{-7} s^{-1}. The results and observations of this work suggest that the AA2219 alloy in T87 temper condition and its friction stir weldment with about 72% joint efficiency produced under optimised processing conditions are not susceptible to SCC in 3.5% NaCl solution.

4. Conclusions

The joining of AA2219-T87 aluminium alloy by friction stir welding could be accomplished with a joint efficiency of around 72%. The weld nugget/TMAZ interface was the weakest region in this weldment in terms of mechanical strength. The general corrosion resistance of the weld nugget was better than that of the parent AA2219 alloy in 3.5% NaCl solution. The increased corrosion resistance of the FSW nugget region was attributed to the dissolution/coarsening of the strengthening precipitates in the nugget region and the consequent reduction in the galvanic drive. The weld nugget exhibited a nobler free corrosion potential compared to the TMAZ/HAZ and the parent alloy had the most active potential. The immersion tests of the weldment in NaCl + H_2O_2 solution revealed that the parent alloy was susceptible to galvanic attack. Nevertheless, the AA2219-T87 parent alloy was not susceptible to SCC in 3.5% NaCl solution at a strain rate of 10^{-6} s^{-1} and 10^{-7} s^{-1} and similar is the case for the friction stir weldments, too. The fracture in the weld nugget/TMAZ interface in the SSRT tests suggested that the failure happens in the softest-region of this weldment. Even though there were some cracks in the weld nugget and TMAZ regions of the weldment when SSRT tested in 3.5% NaCl solution, these developed defects did not inflict any catastrophic SCC failure.

Acknowledgement

The authors gratefully acknowledge Indian Space Research Organization (ISRO) for providing the material for research work and Mr. Rajneesh Kumar (NML, India) for the help in FSW. PBS expresses his sincere thanks to the AvH foundation, Germany for the award of post-doctoral fellowship. KSA gratefully acknowledges the Deutscher Akademischer Austausch Dienst (DAAD) for financial assistance and opportunity to carry out a part of the research work in Germany as a DAAD Fellow.

References

[1] C.J. Dawes, W.M. Thomas, Weld. J. 75 (4) (1996) 41-45.

[2] C. G. Rhodes, M. W. Mahoney, W. H. Bingel, M. Calabrese, Scr. Mater. 48 (2003) 1451-1455.

[3] C. Huang, S. Kou, Weld. J. 80 (1) (2001) 9s-17s.

[4] C. Huang, S. Kou, Weld. J. 80 (2) (2001) 46s-53s.

[5] B.R. Ghosh, R.K. Gupta, S. Biju, P.P. Sinha, J. Solid Mech. Mater. Eng. 1 (2007) 469-479.

[6] K. Srinivasa Rao, G. Madhusudan Reddy, K. Prasad Rao, Mater. Sci. Eng. A 403 (2005) 69-76.

[7] M. Dixit, R.S. Mishra, K.K. Sankaran, Mater. Sci. Eng. A 478 (2008) 163-172.

[8] C.G. Derry, J.D. Robson, Mater. Sci. Eng. A 490 (2008) 328-334.

[9] T.S. Srivatsan, S. Vasudevan, L. Park, Mater. Sci. Eng. A 466 (2007) 235-245.

[10] Y. C. Chen, H. J. Liu, J. C. Feng, J. Mater. Sci. 40 (2005) 4657-4659.

[11] Y. C. Chen, H. J. Liu, J. C. Feng, Mater. Sci. Eng. A 420 (2006) 21-25.

[12] C.S. Paglia, R.G. Buchheit, Mater. Sci. Eng. A 492 (2008) 250-254.

[13] O. Hatamleh, P. M. Singh, H. Garmestani, Corros. Sci. 51 (2009) 135-143.

[14] F. Zucchi, G. Trabanelli, V. Grassi, Mater. Corros. 52 (2001) 853-859.

[15] P.S. Pao, S.J. Gill, C.R. Feng, K.K. Sankaran, Scr. Mater. 45(2001) 605-612.

[16] J. Corral, E.A. Trillo, Y. Li, L.E. Murr, J. Mater. Sci. Lett. 19 (2000) 2117-2122.

[17] P. Bala Srinivasan, W. Dietzel, R. Zettler, J.F. dos Santos, V. Sivan, Mater. Sci. Eng. A 392 (2005) 292-300.

[18] C.S. Paglia, R.G. Buchheit, Scr. Mater. 58 (2008) 383-387.

[19] W. Hu, E.I. Meletis, Mater. Sci. Forum. 331–337 (2000) 1683-1688.

[20] C.S. Paglia, R.G. Buchheit, Mater. Sci. Eng. A 429 (2006) 107-114.

[21] Y. C. Chen, J. C. Feng, H. J. Liu, Mater. Charact. 60 (2009) 476-481.

[22] S.R. Koteswara Rao, G. Madhusudhan Reddy, K. Srinivasa Rao, M. Kamaraj, K. Prasad Rao, Mater. Charact. 55 (2005) 345-354.

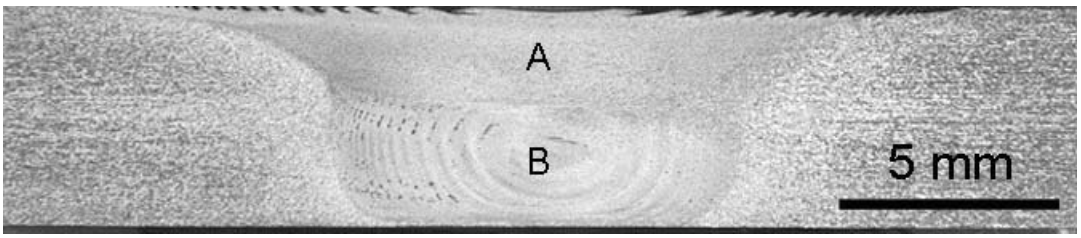

Figure 1 Optical macrograph of the AA2219-T87 friction stir weldment showing the cross-section of nugget.

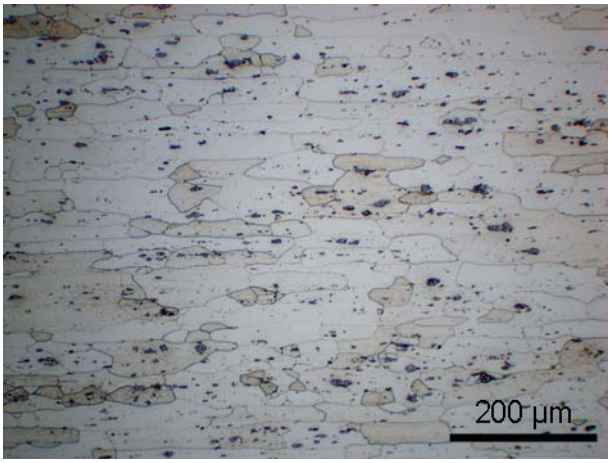

Figure 2 Optical micrograph of the AA2219-T87 parent alloy

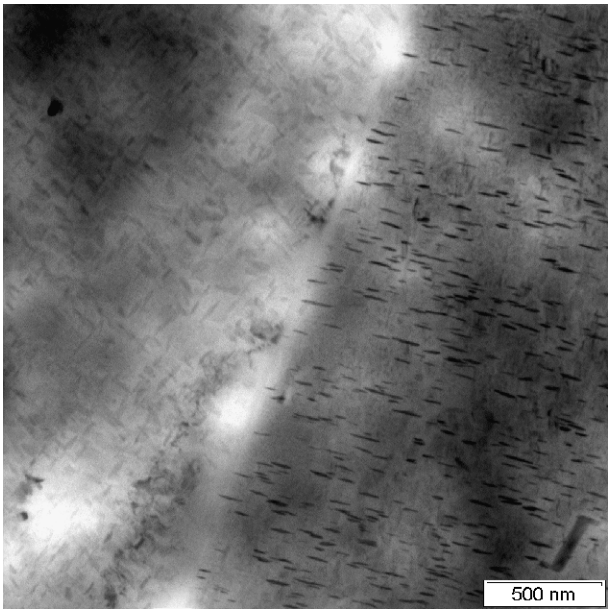

(a) Low magnification

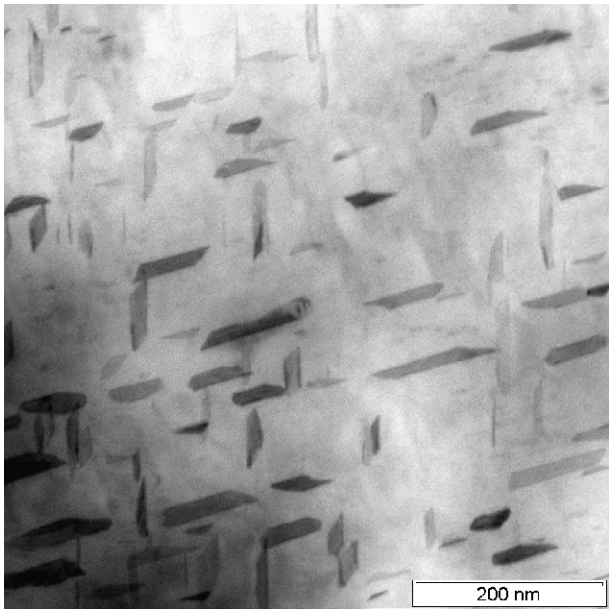

(b) Higher magnification

Figure 3 Transmission electron micrographs of the AA2219-T87 parent alloy

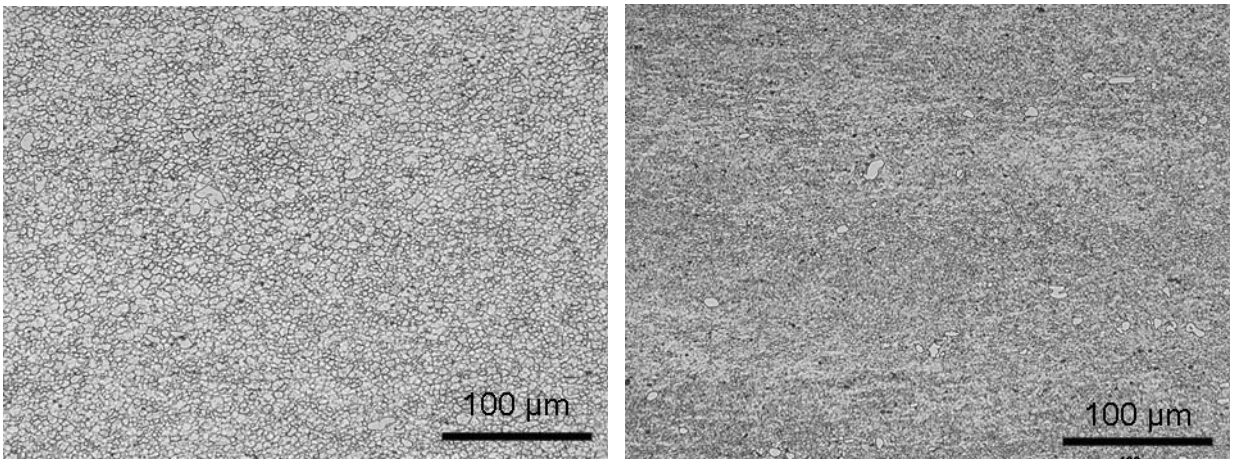

(a) Upper half (marked A in Figure 1) (b) Lower half (marked B in Figure 1)

Figure 4 Optical micrographs showing the re-crystallized grains in the weld nugget

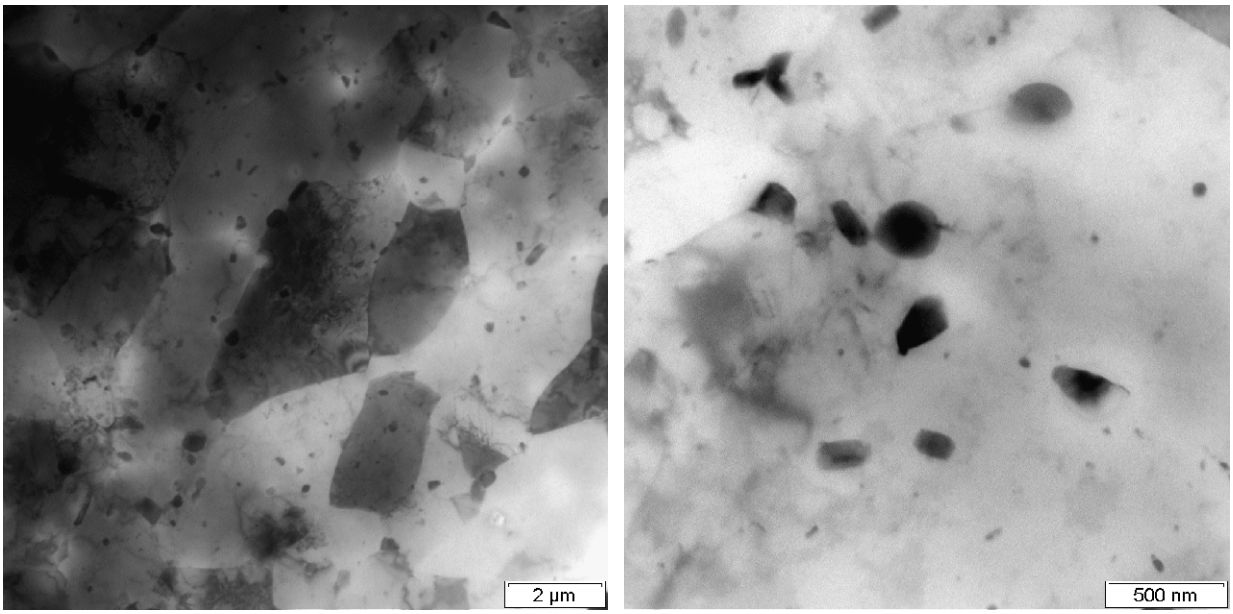

(a) lower magnification (b) higher magnification

Figure 5 Transmission electron micrographs of the weld nugget region

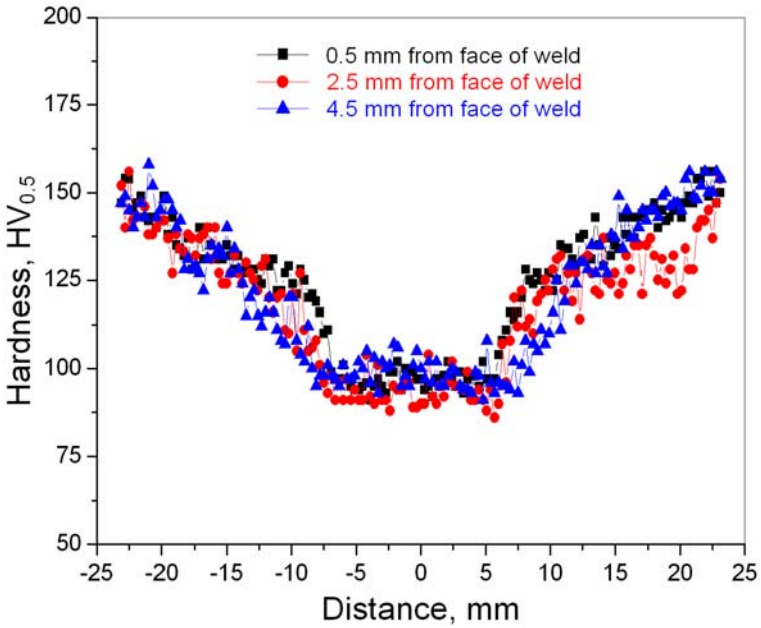

Figure 6 Micro hardness profiles across the friction stir weldment

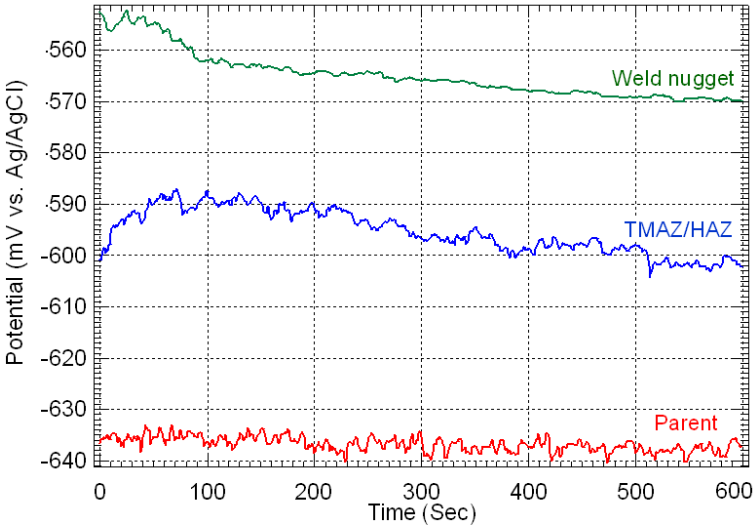

Figure 7(a) Open circuit potentials of the three regions of the friction stir weldment in 3.5% NaCl solution

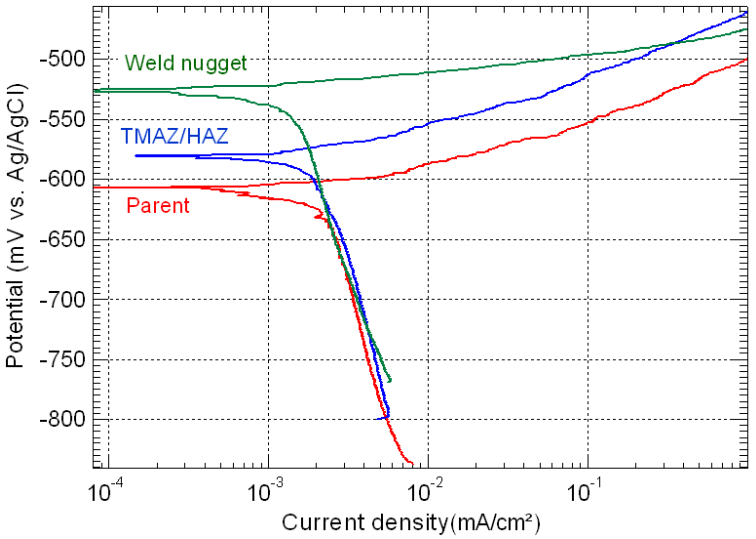

Figure 7(b) Potentiodynamic polarization behaviour of the three different regions of the friction stir weldment in 3.5% NaCl solution

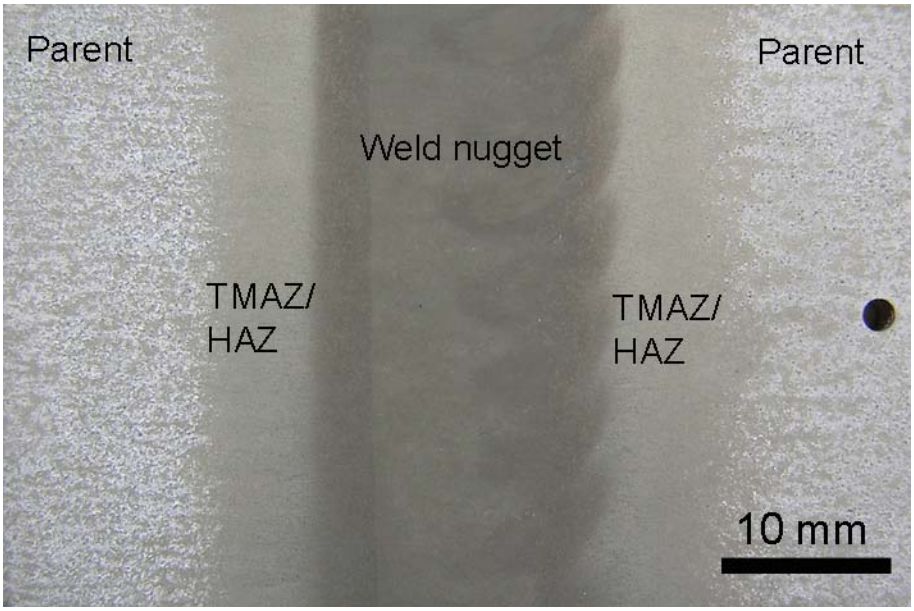

Figure 8 Optical macrograph showing the corrosion damage of the different regions of the friction stir weldment exposed to NaCl + H_2O_2 electrolyte for 6 hours as per ASTM G110

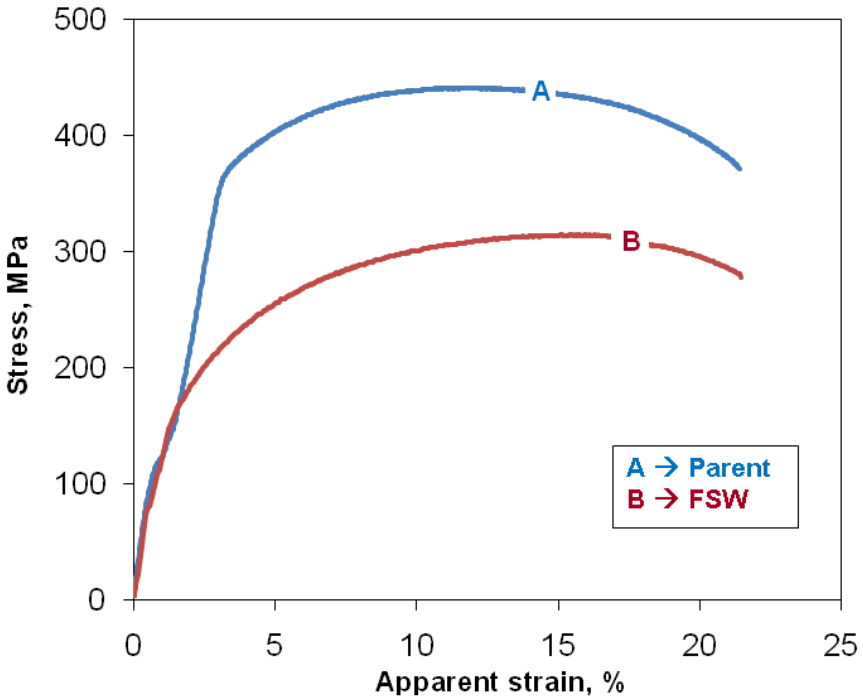

Figure 9 Stress vs. apparent strain plots of the parent alloy and transverse friction stir weldment specimen SSRT tested at a strain rate of 10^{-6} s^{-1} in air

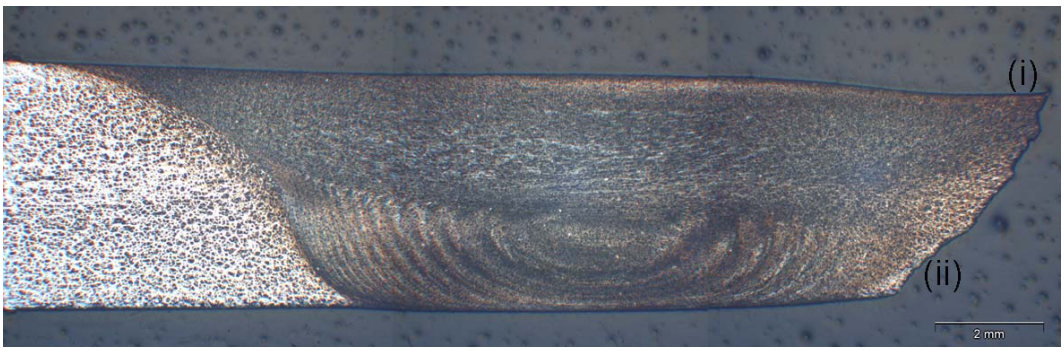

(a)

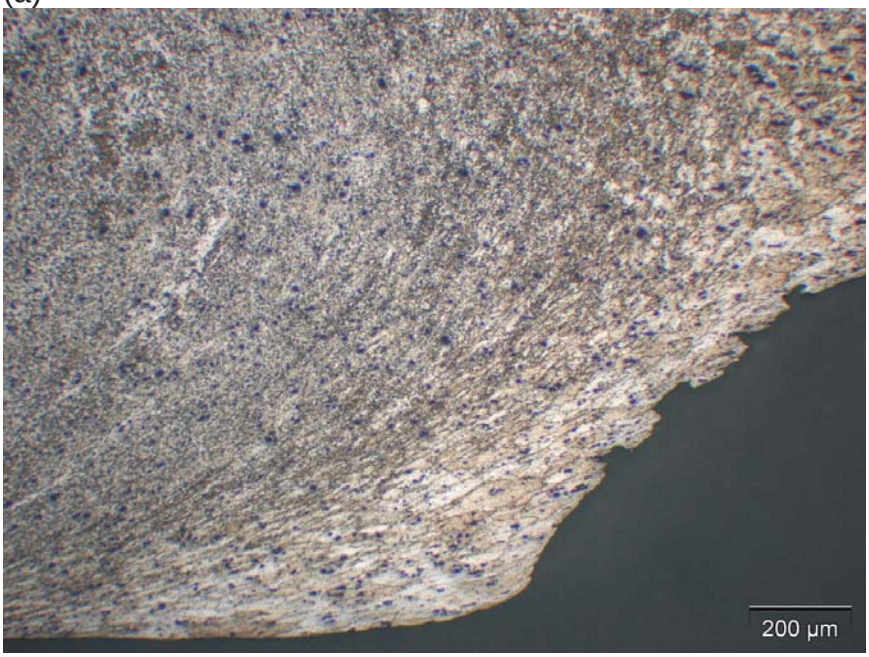

(b)

Figure 10 Optical macrographs of the SSRT tested FSW specimen (in air) showing the fracture location (a) over view (b) higher magnification micrograph

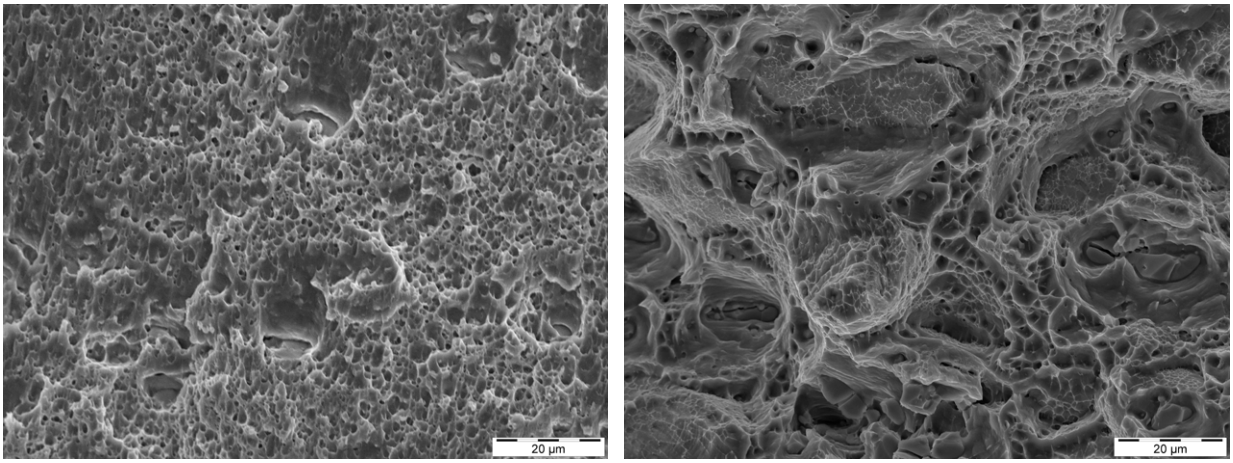

(a) (b)

Figure 11 Scanning electron fractographs of the SSRT tested FSW specimen (in air) at two locations (a) close to the face region of the weld (marked (i) in Figure 10(a) and (b) close to the root region of the weld (marked (ii) in Figure 10a)

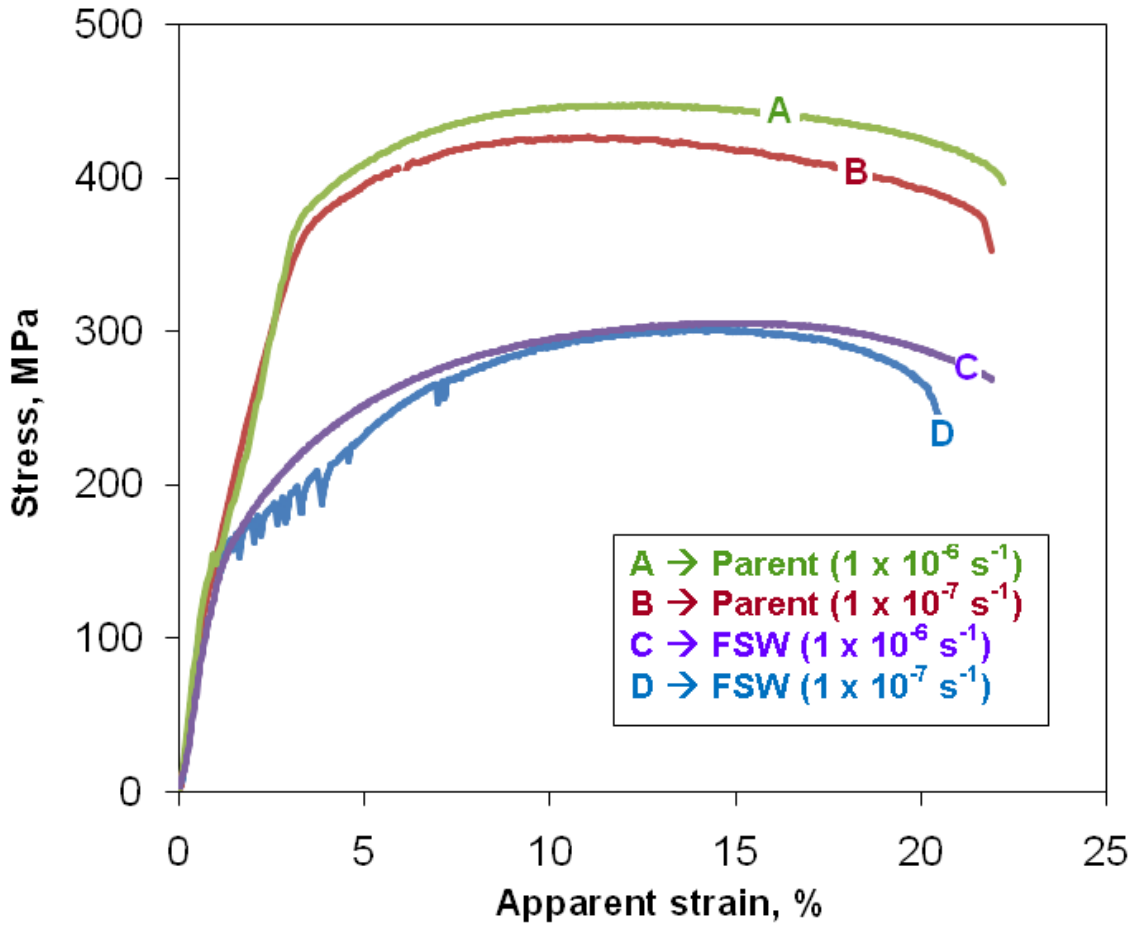

Figure 12 Stress vs. apparent strain plots of the parent and FSW specimens SSRT tested in 3.5% NaCl solution at 10^{-6} s^{-1} and 10^{-7} s^{-1}

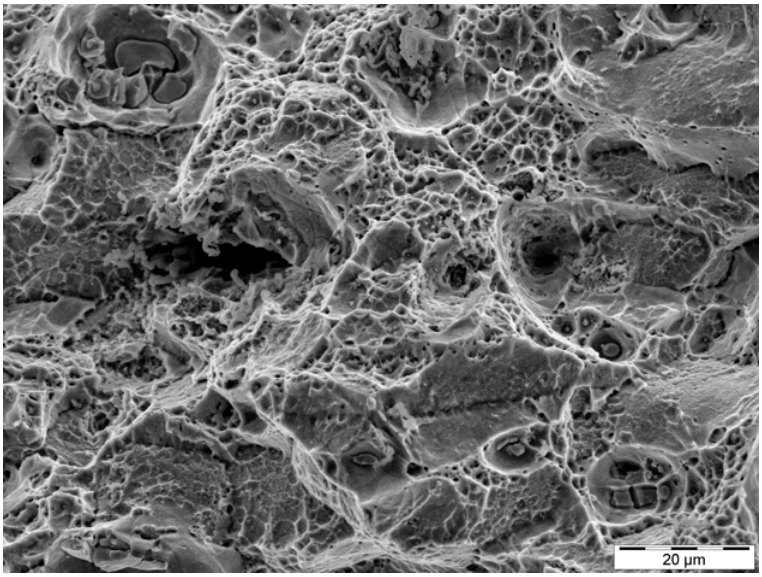

Figure 13 Scanning electron fractograph of the parent alloy SSRT tested in 3.5% NaCl solution at 10^{-7} s^{-1}

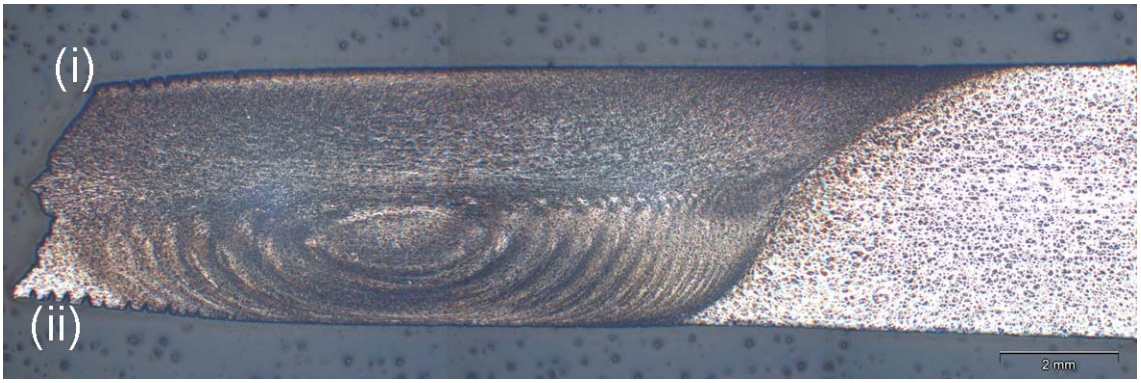

Figure 14 Optical macrograph of the FSW specimen SSRT tested in 3.5% NaCl solution at 10^{-7} s^{-1}

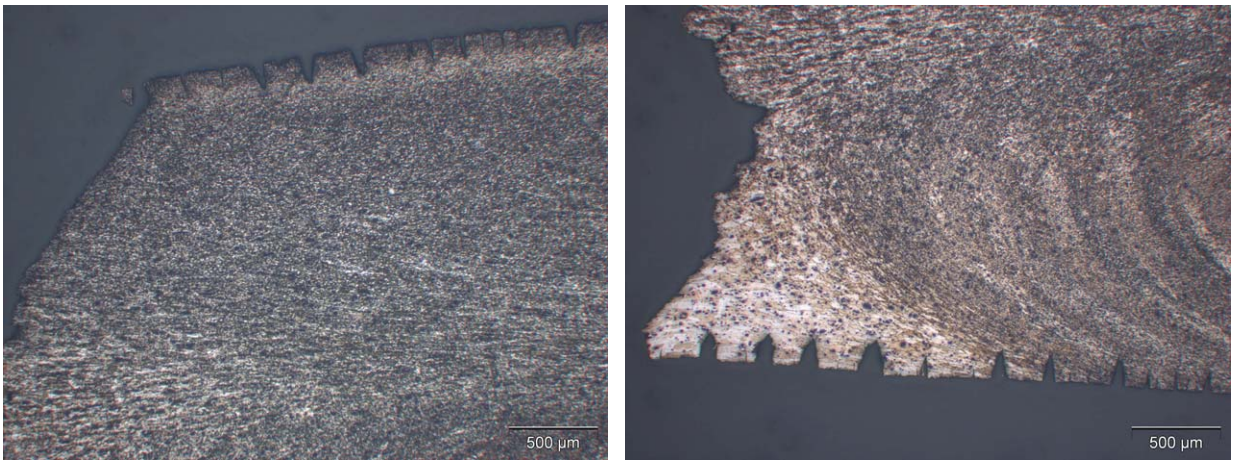

(a) (b)

Figure 15 Higher magnification optical micrographs showing cracks originating from (a) face region and (b) root region of the SSRT tested FSW specimen (regions marked as (i) and (ii), respectively in Figure 14)

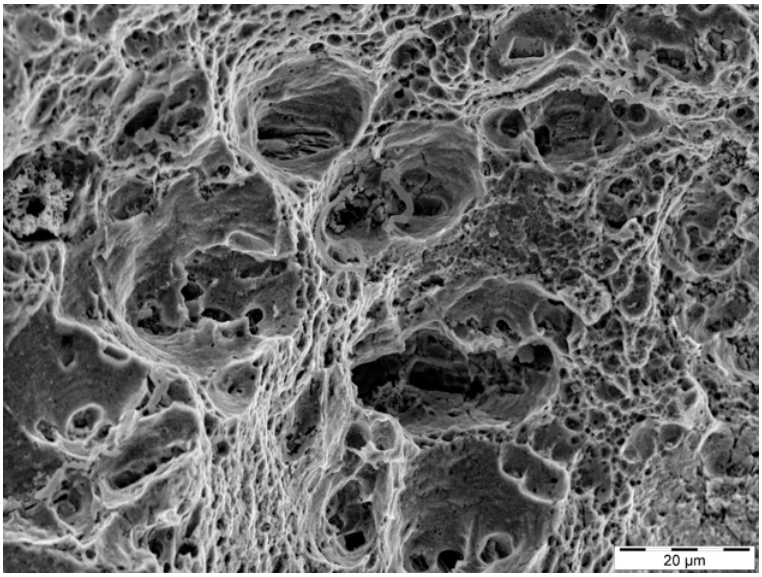

Figure 16 Representative scanning electron fractograph (from the region marked (ii) in Figure 14) of the FSW specimen SSRT tested in 3.5% NaCl solution at 10^{-7} s^{-1}